ACS central science

Research Article

Cite This: ACS Cent. Sci. XXXX, XXX, XXX−XXX

http://pubs.acs.org/journal/acscii

Single Crystals of Electrically Conductive Two-Dimensional Metal−Organic Frameworks: Structural and Electrical Transport Properties

Robert W. Day,[†] D. Kwabena Bediako,[‡,§] Mehdi Rezaee,[∥] Lucas R. Parent,[⊥,▽] Grigorii Skorupskii,[†] Maxx Q. Arguilla,[†] Christopher H. Hendon,[#] Ivo Stassen,[†] Nathan C. Gianneschi,[⊥] Philip Kim,[‡] and Mircea Dincă*[,†]

[†]Department of Chemistry, Massachusetts Institute of Technology, Cambridge, Massachusetts 02138, United States

[‡]Department of Physics and [∥]John A. Paulson School of Engineering and Applied Sciences, Harvard University, Cambridge, Massachusetts 02138, United States

[§]Department of Chemistry, University of California Berkeley, Berkeley, California 94720, United States

[⊥]Department of Chemistry, Materials Science & Engineering, Biomedical Engineering, International Institute for Nanotechnology, Northwestern University, Evanston, Illinois 60208, United States

[▽]Innovation Partnership Building, University of Connecticut, Storrs, Connecticut 06269, United States

[#]Department of Chemistry and Biochemistry, University of Oregon, Eugene, Oregon 97401, United States

Supporting Information

ABSTRACT: Crystalline, electrically conductive, and intrinsically porous materials are rare. Layered two-dimensional (2D) metal−organic frameworks (MOFs) break this trend. They are porous crystals that exhibit high electrical conductivity and are novel platforms for studying fundamentals of electricity and magnetism in two dimensions. Despite demonstrated applications, electrical transport in these remains poorly understood because of a lack of single crystal studies. Here, studies of single crystals of two 2D MOFs, $Ni_3(HITP)_2$ and $Cu_3(HHTP)_2$, uncover critical insights into their structure and transport. Conductivity measurements down to 0.3 K suggest metallicity for mesoscopic single crystals of $Ni_3(HITP)_2$, which contrasts with apparent activated conductivity for polycrystalline films. Microscopy studies further reveal that these MOFs are not isostructural as previously reported. Notably, single rods exhibit conductivities up to 150 S/cm, which persist even after prolonged exposure to ambient conditions. These single crystal studies confirm that 2D MOFs hold promise as molecularly tunable platforms for fundamental science and applications where porosity and conductivity are critical.

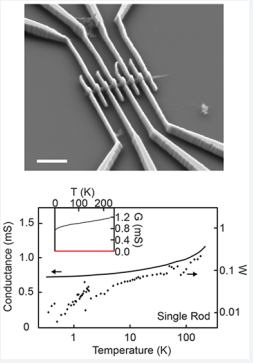

INTRODUCTION

Metal−organic frameworks (MOFs) are hybrid inorganic/organic crystals that can possess features distinct from many crystalline materials:[1,2] intrinsic porosity, nanometer-scale lattice parameters, flexible mechanics, and a rich structural and compositional diversity enabled by advances in both organic and inorganic chemistry in three dimensions. The vast majority of MOFs are insulators and have been used in applications that benefit from high surface areas and a chemical tunability, such as gas capture and catalysis.[1] Conductive MOFs[3,4] represent a new type of hybrid inorganic/organic conductor in addition to nonporous coordination polymers and hybrid perovskites, which have recently demonstrated high conductivities and superconductivity[5] and promising performances for optoelectronics,[6] respectively.

Two-dimensional (2D) layered MOFs,[7−19] where metals and redox-active ligands form extended π−d conjugated sheets (Figure 1), have shown the highest conductivities and are predicted to exhibit rare transport phenomena including, for instance, the quantum anomalous hall effect.[11] However, because of poor synthetic control and small crystallite size, charge transport and structural studies for the 2D MOFs have generally relied on polycrystalline films/pellets and powder X-ray diffraction (PXRD), where grain boundaries and anisotropy obscure the intrinsic properties. Only a handful of single crystal devices have been reported including a room-temperature conductivity value for a 2D MOF,[19] for a 2D coordination polymer,[20] and for some less-conductive three-dimensional (3D) MOFs.[21,22] Despite Ni_3(2,3,6,7,10,11-hexaiminotriphenylene)$_2$ ($Ni_3(HITP)_2$) possessing one of the highest conductivities for a porous MOF and having demonstrated promise for various applications, its conduction is poorly understood; calculations have predicted $Ni_3(HITP)_2$ to be metallic, but results of experiments on polycrystalline pellets down to 80 K have been interpreted as semiconducting.[8,23] Here, with isolated crystals, we reveal the distinct layer stacking for $Ni_3(HITP)_2$ and Cu_3(2,3,6,7,10,11-hexahydroxytriphenylene)$_2$ ($Cu_3(HHTP)_2$), the metallic nature of single crystals of $Ni_3(HITP)_2$, and the importance of

Received: October 2, 2019

DOI: 10.1021/acscentsci.9b01006
ACS Cent. Sci. XXXX, XXX, XXX−XXX

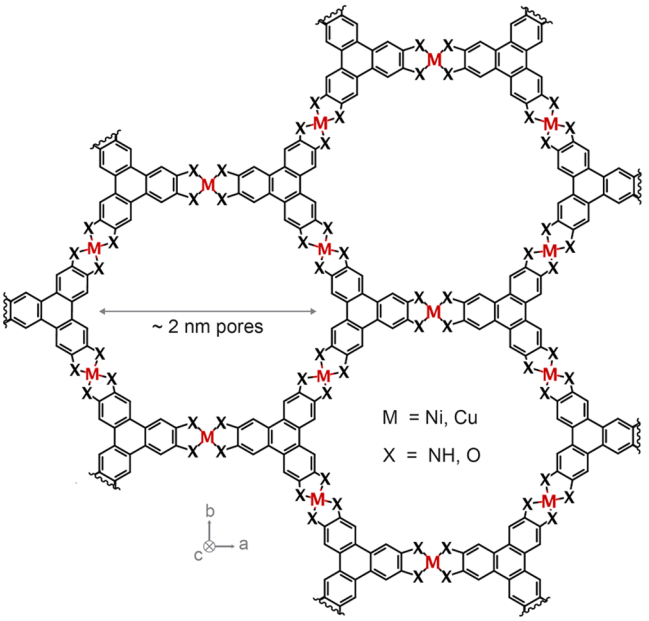

Figure 1. Porous, conductive 2D MOFs. Schematic illustrating the general structure of conductive 2D MOFs where layers stack in the *c* direction to form intrinsically porous crystals with pores of approximately 2 nm in diameter. Metal atoms and organic ligands comprise the honeycomb lattice of the 2D layers. $Ni_3(HITP)_2$ and $Cu_3(HHTP)_2$ have M/X = Ni/NH and Cu/O respectively.

transport in the out-of-plane direction despite the presumed dominance of in-plane transport for 2D MOFs.

RESULTS AND DISCUSSION

To understand charge transport in our 2D MOFs, we isolated individual crystals of $Ni_3(HITP)_2$ and measured their conductivity as a function of temperature (Figure 2). Published conditions[8] generate an interconnected nanocrystalline morphology (Figure S1), which has been challenging to isolate crystals from. Here, we obtain isolated rods of $Ni_3(HITP)_2$ up to ~2 μm in length and ~200 nm in diameter (see Methods and Figure S1). Devices were fabricated by drop-casting suspensions of $Ni_3(HITP)_2$ rods onto Si covered by SiO_2 substrates and using electron-beam lithography and metal evaporation to deposit Ti/Pd contacts on top of the rods (Figure 2a; see Methods). A DC current−voltage (I−V) sweep for a representative device (Figure 2b) yielded four-probe conductance values *G* of 1.3 mS at 295 K and 0.7 mS at 1.4 K, and two-probe values of 0.25 mS at 295 K and 0.13 mS at 1.4 K. The linearity observed in these DC measurements even at small biases evinces ohmic contacts over this temperature range and validates the use of AC transport measurements for variable temperature (VT) and magnetic field-dependence studies. A reversible decrease in conductance is observed when a magnetic field is applied (Figure 2b, inset), and the magnitude of this change decreases as the temperature *T* increases from 1.4 K (top) to 10 K (bottom). The positive magnetoresistance that is enhanced at low temperature suggests a shrinking of electronic impurity wave function under a magnetic field.[24] However, because our current device geometry allows for potential mixing between Hall and longitudinal resistance, pinning the exact origin of this behavior will require multiterminal magnetotransport studies in the future.

We find that further decreasing the temperature from 1.4 to 0.3 K (Figure 2c; solid line, left axis) decreased the four-probe conductance negligibly. VT measurements on three additional $Ni_3(HITP)_2$ rod devices showed a similar weak, positive dependence on temperature (Figure S2). In contrast, a four-probe VT measurement of a polycrystalline $Ni_3(HITP)_2$ film device (Figure 2d; black solid line, left axis) revealed a

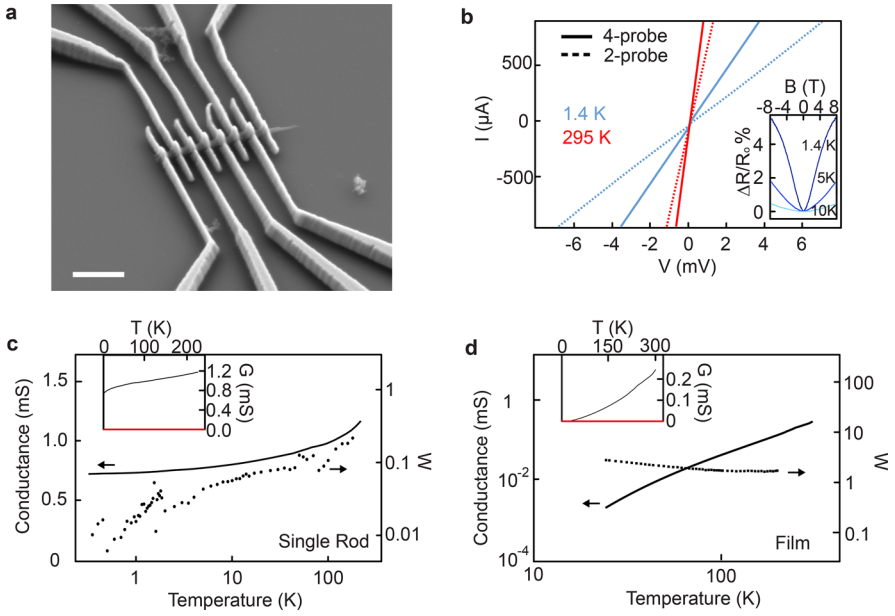

Figure 2. Conductive 2D MOF devices of $Ni_3(HITP)_2$. (a) SEM of a single rod $Ni_3(HITP)_2$ device with Ti/Pd contacts. Scale bar, 1 μm. (b) Current−voltage plots of a single rod $Ni_3(HITP)_2$ device at 295 K (red) and 1.4 K (blue). Inset: Normalized magnetoresistance at several fixed temperatures. (c, d) 4-probe temperature-dependent conductance (solid line; left axis) of a single rod device (c) and a polycrystalline film device (d) of $Ni_3(HITP)_2$ and their corresponding Zabrodskii plots with their reduced activation energy (dotted lines; right axes). Inset: Temperature-dependent conductance plotted with linear axes.

DOI: 10.1021/acscentsci.9b01006
ACS Cent. Sci. XXXX, XXX, XXX−XXX

conductance that decreased by orders of magnitude over a smaller temperature range.

To understand the VT behavior for these single rod and polycrystalline devices, we plot $W(T) = \mathrm{d}\ln G/\mathrm{d}\ln T$ against T in a logarithmic scale as shown in Figure 2c,d (dashed lines, right axes). This Zabrodskii plot scheme[25] has been used for doped organic polymers,[26] quantum dot films,[27] and other systems,[28,29] where the negative slope of the Zabrodskii plot indicates localization behaviors with a reduced activation gap. We observe a positive slope for all single rod devices, indicating metallicity in the absence of the strong localization at low temperatures. A small reduced activation energy value that decreases as temperature decreases is consistent with a nonzero conductance value as T goes to 0 K (Figure 2c inset). For the polycrystalline film device, we observe a negative slope in the Zabrodskii plot, indicating a semiconducting nature, where the conductance approaches 0 as T goes to 0 K (Figure 2d inset). Literature precedence[27−29] and additional data (Figure S3 and S4) are consistent with our interpretation of metallicity or degenerate doping in $Ni_3(HITP)_2$ (see Supplementary Discussion).

We also isolated individual crystals of $Cu_3(HHTP)_2$ and measured their conductivities as previous reports have indicated $Cu_3(HHTP)_2$ to be isostructural to $Ni_3(HITP)_2$.[18] For $Cu_3(HHTP)_2$, thin nanocrystalline films[18] or rods with diameters of ∼100 nm have been reported.[19] Here, we obtain rods (Figure 3a) or particles (Figure 3b) of $Cu_3(HHTP)_2$ with six-sided cross sections whose widths can be controlled synthetically (see Methods) from 100 nm up to 5 μm (Figure S5). We also obtain thin flakes of $Cu_3(HHTP)_2$ via techniques used to exfoliate traditional 2D materials. Sonication of washed $Cu_3(HHTP)_2$ powder in isopropanol, water, or acetonitrile for 1−2 h, followed by centrifugation and isolation of the suspended blue supernatant yields flakes with widths of ∼1 μm, and heights of ∼50−500 nm as evidenced by scanning electron microscope (SEM) and atomic force microscope (AFM) (Figure S6).

$I-V$ curves for $Cu_3(HHTP)_2$ rod and exfoliated flake devices (Figure 3c), whose SEM images are shown as insets, yielded resistances of 562 kΩ and 84 kΩ at 295 K, allowing us to estimate conductivities of 1.5 S/cm and 0.5 S/cm, respectively, for these devices (Figure S7). Pellet conductivities of 0.1 S/cm and 0.09 S/cm were obtained from the $Cu_3(HHTP)_2$ batch of particles used to exfoliate flakes, and the $Cu_3(HHTP)_2$ rod batch, respectively. We note that we observe more variability in conductivity for $Cu_3(HHTP)_2$ devices than for $Ni_3(HITP)_2$ devices, which is likely related to difficulties with reliably forming ohmic contacts to $Cu_3(HHTP)_2$, as indicated by the nonlinear $I-V$ curves observed for some devices as well as a significant decrease in conductance from 300 to 200 K, which prevents low temperature characterization. Despite the contact variability, over 10 single rod devices for $Cu_3(HHTP)_2$ from different synthetic batches put a lower limit of conductivity at ∼0.1 S/cm and indicate that in-plane and out-of-plane conductivities are of comparable orders of magnitude.

We performed high resolution (HR) TEM on individual crystals of $Ni_3(HITP)_2$ and $Cu_3(HHTP)_2$ to characterize their respective lattice structures, revealing key new insights into the stacking of 2D layers. These and other triphenylene-based MOFs have been reported to be nearly isostructural based on similarities in PXRD patterns, but the true nature of the stacking remained unclear.[18] Imaging perpendicular to the long

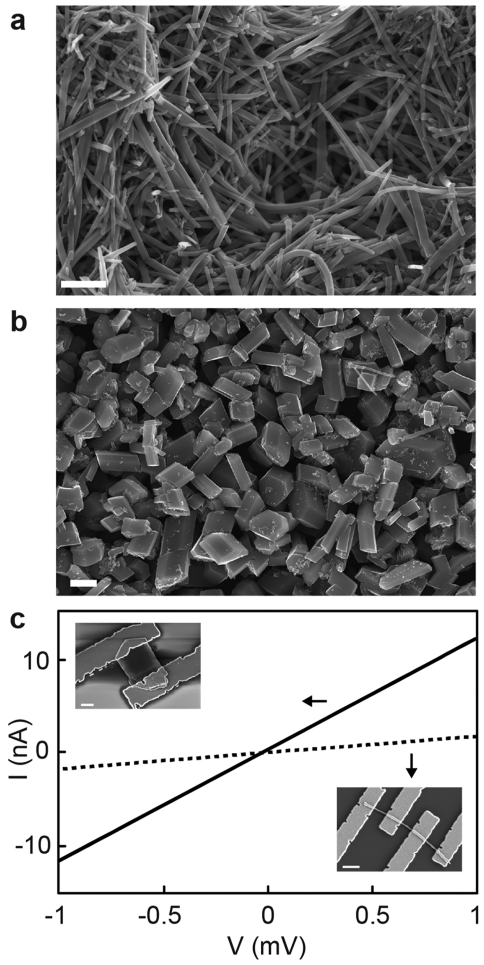

Figure 3. $Cu_3(HHTP)_2$. (a, b) SEM images of $Cu_3(HHTP)_2$ rods (a) and particles (b) obtained using distinct synthetic conditions (see Methods). Scale bars, 1 μm. (c) Room temperature $I-V$ curves of an exfoliated $Cu_3(HHTP)_2$ flake (solid line) and $Cu_3(HHTP)_2$ rod (dashed line) at 295 K. Insets show SEM images for corresponding devices.

axis of a $Ni_3(HITP)_2$ rod (Figure 4a, left) reveals contrast fringes that run approximately parallel to the rod's axis. The fast Fourier transforms (FFTs) for this rod (Figure 4a, middle) and others (Figure S8) show the fringe periodicity to be 1.8 nm (red arrows), 0.9 nm (orange arrow), and 0.6 nm (blue arrow). Further inspection indicates an additional periodic feature (diffuse spot) with a spacing of 0.33 nm (white arrow) but with an orientation that is nearly perpendicular to the 1.8 nm family of fringes. The orthogonality of these spots in the FFT, combined with the periodic intensity profile (Figure 4a, bottom) across the width of the rod, suggests that the 2D layers stack in an eclipsed or near-eclipsed configuration, which we illustrate schematically in Figure 4a, right. Specifically, the darker fringes (global minima in intensity profile) correspond to electron scattering along a higher metal and ligand density pathway, and the brighter fringes (local minima) to a lower density scattering pathway along the pore's center. The brightest fringes (global maxima) arise from scattering along vectors completely free of metal (Ni) atoms. PXRD and additional TEM data from other zone axis (Figure S9), which show 1.1 nm spaced fringes and a hexagonal lattice, support this structural model (Figure 4a).

DOI: 10.1021/acscentsci.9b01006
ACS Cent. Sci. XXXX, XXX, XXX−XXX

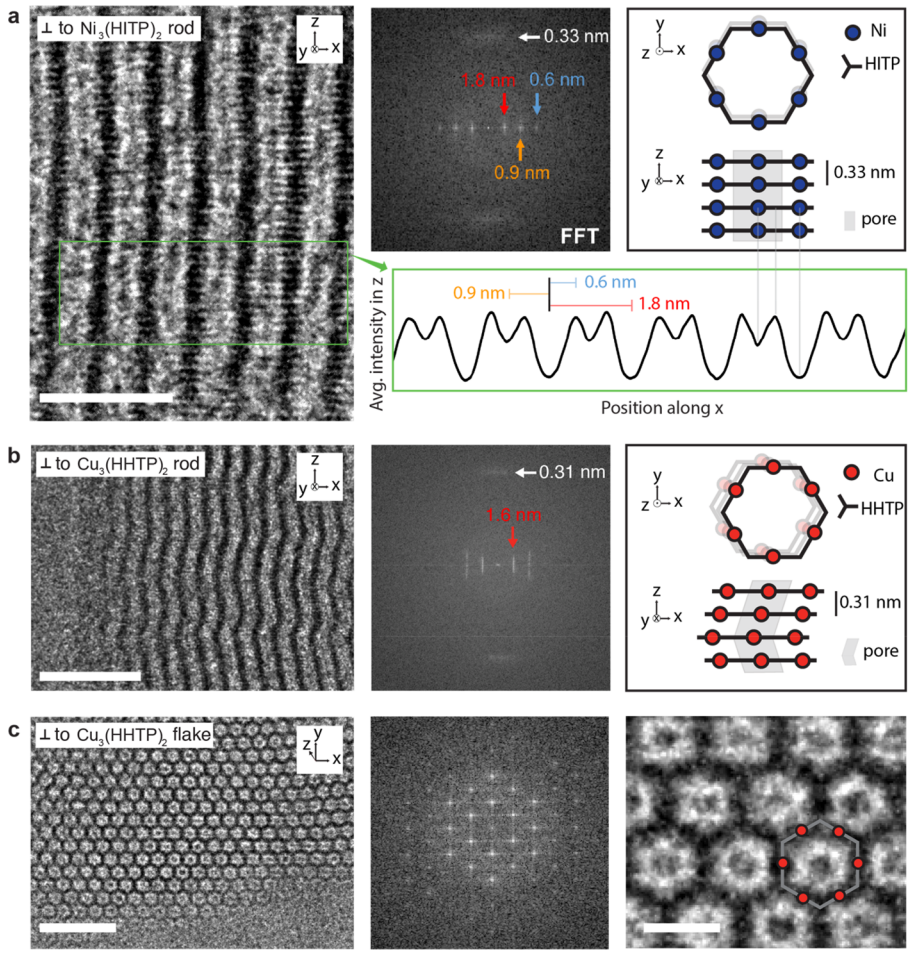

Figure 4. TEM of $Ni_3(HITP)_2$ and $Cu_3(HHTP)_2$. (a) Left: HRTEM image of a $Ni_3(HITP)_2$ rod whose long axis lies along the *z*-direction. Middle: FFT from a lower-magnification TEM image. Right: Schematic of $Ni_3(HITP)_2$ structure illustrated for four layers in a near-eclipsed stacking configuration for imaging perpendicular (top schematic) and parallel (bottom schematic) to the 2D layers. Bottom: average intensity in the *z*-direction measured along the *x*-direction from the green box in the HRTEM image. The periodic features seen in the FFT are indicated with the red, orange, and blue lines. The gray lines extending from the intensity profile to the schematic indicate the pathways giving rise to the observed intensity profile. Scale bar, 5 nm. (b) Left: HRTEM image of a $Cu_3(HHTP)_2$ rod whose long axis lies along the *z*-direction. Middle: FFT from a lower-magnification TEM image. Right: Schematic of the $Cu_3(HHTP)_2$ structure illustrated for four layers in a near-eclipsed stacking configuration for imaging perpendicular (top schematic) and parallel (bottom schematic) to the 2D layers. The three top layers are depicted as stacked with an offset along the same direction, while the bottom layer is stacked with an offset in the opposite direction, and represents a stacking fault. Scale bar, 10 nm. (c) Low- (left) and high-magnification (right) HRTEM image of $Cu_3(HHTP)_2$ flake obtained after exfoliation of $Cu_3(HHTP)_2$ particles. Scale bars, 10 nm (left) and 2 nm (right).

Surprisingly, HRTEM imaging perpendicular to the long axis of a $Cu_3(HHTP)_2$ crystal, previously reported as isostructural with $Ni_3(HITP)_2$,[18] and FFT analysis (Figure 4b; Figure S10) reveals a critical difference in the nature of stacking in $Cu_3(HHTP)_2$ compared to that of $Ni_3(HITP)_2$. That is, the eclipsed stacking model does not fit. For $Cu_3(HHTP)_2$, the 2D layers are oriented horizontally and perpendicular to the rod axis (i.e., stacked from top to bottom in Figure 4b, left), evidenced by the vertical position of the 0.31 spots in the FFT (white arrow). However, the angled orientation of the bright fringes in the HRTEM images indicates that the 2D layers are not oriented perpendicular to the pores axis. HRTEM and FFTs from other $Cu_3(HHTP)_2$ rods (Figure S11) confirm this finding and suggest that the stacking orientation is tilted approximately 15−23° from a direction perpendicular to the pore axis. We propose that angled pores can arise by stacking subsequent layers with an offset along the same *a*/*b* direction (Figure 4b, right). Furthermore, the back-and-forth undulating nature of the pores observed in some rods (Figure 4b, left) and the smearing of spots into lines in their respective FFTs (Figure 4b, middle) can be explained by stacking faults or twin defects, as shown schematically with the bottom layer (Figure 4b, right and Figure S10). Such defects would give rise to reversals in the stacking offset direction and thus an undulating appearance. Additional data are consistent with this model where layers and pores are not perpendicular because of noneclipsed stacking. First, SEM images of larger, faceted rods show six-sided cross sections that are not perpendicular to the rod's long axis, with clean cleavage planes that are similarly not normal to the rod's long axis (Figure S12). Second, synchrotron PXRD data of $Cu_3(HHTP)_2$ (Figure S13) do not fit well with an eclipsed hexagonal unit cell but rather by a structure similar to the one outlined above (Figure 4b, right). Third, TEM images (Figure 4c, left) and FFTs (Figure 4c, middle) of thin flakes obtained after exfoliation show a hexagonal crystalline structure with a honeycomb pattern that is consistent with imaging parallel to the pore axis (~20° from the *z*-direction).

DOI: 10.1021/acscentsci.9b01006
ACS Cent. Sci. XXXX, XXX, XXX−XXX

Further analysis and literature precedent suggest new insights into the 2D layer stacking that may be relevant to the growth, transport, and calculations thereof for 2D MOFs generally. The diffuse nature of the interlayer spots in the FFT for $Ni_3(HITP)_2$ (white arrow; Figure 4a, middle) and the range of pore angles for some $Cu_3(HHTP)_2$ rods (Figure 4b, middle) are consistent with a variation in the stacking offset between layers and may indicate that a strict assignment of AA or AB stacking with a single offset value may not fully capture the structural features normal to the 2D MOF plane. Furthermore, the pores can stay continuous over hundreds of nanometers despite significant stacking variation over that length scale, indicating that the 2D layers are strongly ordered locally, where each subsequent layer is only offset by a small fraction of the 2D lattice's unit cell. This is consistent with previous calculations for $Ni_3(HITP)_2$,[8] which predict a shallow potential energy surface for various stacking configurations that are near but not perfectly eclipsed (Figures S8 and S10).

With the aid of single crystal device data, we make observations relevant to understanding transport in conductive 2D MOFs. First, for both $Cu_3(HHTP)_2$ and $Ni_3(HITP)_2$ systems, rod devices with significant out-of-plane contributions show conductivities greater than their polycrystalline pellet measurements. The out-of-plane transport is often disregarded in the literature compared to in-plane transport[30] but is consistent with band structure and density of states calculations, which show that C, N, and Ni contribute to these out-of-plane bands. Second, Zabrodskii plots show a positive slope for single crystal $Ni_3(HITP)_2$ devices but a negative slope for its polycrystalline film, indicating the intrinsic metallic nature for single crystal MOFs, with the observed nonmetallic behavior of polycrystalline film likely extrinsic to the materials. Additional work is needed to further understand the role that anisotropy and grain boundaries contribute to polycrystalline transport. Importantly, for organic systems and quantum dot films, by controlling film preparation and the material's surface, conductance can be increased by orders of magnitude; similar strategies may yield significant increases in polycrystalline MOF transport. Last, we note that literature reports have attempted to claim metallicity or a semiconducting nature for various MOFs or coordination polymers by analyzing high temperature polycrystalline pellets or by applying Arrhenius equations to weak temperature dependences, which may lead to incorrect interpretations of small band gaps. We show that, although the out-of-plane conduction for $Ni_3(HITP)_2$ devices decreases with temperature, the Zabrodskii analysis at low temperatures and single crystals are critical in determining the nature of its conduction.

■ ASSOCIATED CONTENT

Supporting Information

The Supporting Information is available free of charge at https://pubs.acs.org/doi/10.1021/acscentsci.9b01006.

Material preparation and characterization, device fabrication and characterization, band structure calculations, and growth and device discussions (PDF)

■ AUTHOR INFORMATION

Corresponding Author

*E-mail: mdinca@mit.edu.

ORCID

Christopher H. Hendon: 0000-0002-7132-768X

Ivo Stassen: 0000-0003-3997-653X

Nathan C. Gianneschi: 0000-0001-9945-5475

Mircea Dincă: 0000-0002-1262-1264

Notes

The authors declare no competing financial interest.

■ ACKNOWLEDGMENTS

Work in the Dincă lab was supported by the Army Research Office (Grant No. W911NF-17-1-0174). P.K. acknowledges the support from ONR MURI (N00014-16-1-2921) for electrical transport measurement and ARO (W911NF-18-1-0366) for device fabrication. N.C.G. acknowledges support from ARO (W911NF-181-0359). I.S. is grateful to the Belgian American Educational Foundation (BAEF) and Research Foundation − Flanders (FWO) for postdoctoral fellowships. Computational work used the Extreme Science and Engineering Discovery Environment (XSEDE), which is supported by the National Science Foundation Grant No. ACI-1548562, and the PICS machine, Coeus, which is supported by the NSF (DMS1624776). TEM characterization was performed in the EPIC facility of Northwestern University's NUANCE Center, which has received support from the Soft and Hybrid Nanotechnology Experimental (SHyNE) Resource (NSF ECCS-1542205); the MRSEC program (NSF DMR-1121262) at the Materials Research Center; the International Institute for Nanotechnology (IIN); the Keck Foundation; and the State of Illinois, through the IIN. Part of this work was performed at the Center for Nanoscale Systems (CNS), a member of the National Nanotechnology Coordinated Infrastructure Network, which is supported by the National Science Foundation under NSF award #1541959. CNS is part of Harvard University.

■ REFERENCES

(1) Furukawa, H.; et al. The Chemistry and Applications of Metal-Organic Frameworks. *Science* **2013**, *341*, 1230444.

(2) Coudert, F.-X. Responsive Metal-Organic Frameworks and Framework Materials: Under Pressure, Taking the Heat, in the Spotlight, with Friends. *Chem. Mater.* **2015**, *27*, 1905−1916.

(3) Stassen, I.; et al. An Updated Roadmap for the Integration of Metal-Organic Frameworks with Electronic Devices and Chemical Sensors. *Chem. Soc. Rev.* **2017**, *46*, 3185−3241.

(4) Sun, L.; Campbell, M. G.; Dincă, M. Electrically Conductive Porous Metal-Organic Frameworks. *Angew. Chem., Int. Ed.* **2016**, *55*, 3566.

(5) Huang, X.; et al. Superconductivity in a Copper(II)-Based Coordination Polymer with Perfect Kagome Structure. *Angew. Chem., Int. Ed.* **2018**, *57*, 146−150.

(6) Li, W.; Wang, Z.; Deschler, F.; Gao, S.; Friend, R. H.; Cheetham, A. K. Chemically Diverse and Multifunctional Hybrid Organic-Inorganic Perovskites. *Nat. Rev. Mater.* **2017**, *2*, 16099.

(7) Ko, M.; Mendecki, L.; Mirica, K. Conductive Two-Dimensional Metal-Organic Frameworks as Multifunctional Materials. *Chem. Commun.* **2018**, *54*, 7873−7891.

(8) Sheberla, D.; et al. High Electrical Conductivity in Ni_3(2,3,6,7,10,11- hexaiminotriphenylene)$_2$, a Semiconducting Metal-Organic Graphene Analogue. *J. Am. Chem. Soc.* **2014**, *136*, 8859−8862.

(9) Dou, J.-H.; et al. Signature of Metallic Behavior in the Metal-Organic Frameworks M_3(hexaiminobenzene)$_2$. *J. Am. Chem. Soc.* **2017**, *139*, 13608−13611.

(10) Campbell, M. G.; et al. Cu_3(hexaiminotriphenylene)$_2$: an Electrically Conductive 2D Metal-Organic Framework for ChemiresistiveSensing. *J. Am. Chem. Soc.* **2015**, *137*, 13780.

DOI: 10.1021/acscentsci.9b01006
ACS Cent. Sci. XXXX, XXX, XXX−XXX

(11) Dong, L.; et al. Two-Dimensional π-Conjugated Covalent-Organic Frameworks as Quantum Anomalous Hall Topological Insulators. *Phys. Rev. Lett.* **2016**, *116*, 096601.
(12) Dong, R.; Zhang, Z.; Tranca, D. C.; et al. A Coronene-Based Semiconducting Two-Dimensional Metal-Organic Framework with Ferromagnetic Behavior. *Nat. Commun.* **2018**, *9*, 2637.
(13) Sheberla, D.; et al. Conductive MOF Electrodes for Stable Supercapacitors with High Areal Capacitance. *Nat. Mater.* **2017**, *16*, 220−224.
(14) Feng, D.; et al. Robust and Conductive Two-Dimensional Metal-Organic Frameworks with Exceptionally High Volumetric and Areal Capacitance. *Nature Energy* **2018**, *3*, 30−36.
(15) Miner, E. M.; Fukushima, T.; Sheberla, D.; Sun, L.; Surendranath, Y.; Dincă, M. Electrochemical Oxygen Reduction Catalysed by Ni_3(hexaiminotriphenylene)$_2$. *Nat. Commun.* **2016**, *7*, 10942.
(16) Dong, R.; Han, P.; Arora, H.; et al. High-Mobility Band-Like Charge Transport in a Semiconducting Two-Dimensional Metal-Organic Framework. *Nat. Mater.* **2018**, *17*, 1027−1032.
(17) Campbell, M. G.; Liu, S. F.; Swager, T. M.; Dincă, M. Chemiresistive Sensor Arrays from Conductive 2D Metal-Organic Frameworks. *J. Am. Chem. Soc.* **2015**, *137*, 13780−13783.
(18) Rubio-Giménez, V.; et al. Bottom-Up Fabrication of Semiconductive Metal-Organic Framework Ultrathin Films. *Adv. Mater.* **2018**, *30*, 1704291.
(19) Hmadeh, M.; et al. New Porous Crystals of Extended Metal-Catecholates. *Chem. Mater.* **2012**, *24*, 3511−3513.
(20) Kambe, T.; et al. Redox Control and High Conductivity of Nickel Bis(dithiolene) Complex π-Nanosheet: A Potential Organic Two-Dimensional Topological Insulator. *J. Am. Chem. Soc.* **2014**, *136*, 14357−14360.
(21) Aubrey, M.; et al. Electron Delocalization and Charge Mobility as a Function of Reduction in a Metal-Organic Framework. *Nat. Mater.* **2018**, *17*, 625−632.
(22) Xie, L. S.; et al. Tunable Mixed-Valence Doping toward Record Electrical Conductivity in a Three-Dimensional Metal-Organic Framework. *J. Am. Chem. Soc.* **2018**, *140*, 7411−7414.
(23) Foster, M. E.; et al. Unraveling the Semiconducting/Metallic Discrepancy in Ni_3(HITP)$_2$. *J. Phys. Chem. Lett.* **2018**, *9*, 481−486.
(24) Nguen, V. L.; Spivak, B. Z.; Shklovskii, B. I. Tunnel Hops in Disordered Systems. *Sov. Phys.-JETP* **1985**, *62*, 1021.
(25) Zabrodskii, A. G.; Shlimak, I. S. *Sov. Phys. Semicond.* **1975**, *9*, 391.
(26) Le, T.-H.; Kim, Y.; Yoon, H. Electrical and Electrochemical Properties of Conducting Polymers. *Polymers* **2017**, *9*, 150.
(27) Liu, H.; Pourret, A.; Guyot-Sionnest, P. Mott and Efros-Shklovskii Variable Range Hopping in CdSe Quantum Dots Films. *ACS Nano* **2010**, *4*, 5211−5216.
(28) Ahlskog, M.; Reghu, M.; Heeger, A. J. The Temperature Dependence of the Conductivity in the Critical Regime of the Metal-Insulator Transition in Conducting Polymers. *J. Phys.: Condens. Matter* **1997**, *9*, 4145−4156.
(29) Kaiser, A. B. Electronic Transport Properties of Conducting Polymers and Carbon Nanotubes. *Rep. Prog. Phys.* **2001**, *64*, 1−49.
(30) Skorupskii, G.; Trump, B. A.; Kasel, T. W.; Brown, C. M.; Hendon, C. H.; Dincă, M. Efficient and tunable one-dimensional charge transport in layered lanthanide metal-organic frameworks *Nat. Chem.*, **2019**, *11*, DOI: 10.1038/s41557-019-0372-0

DOI: 10.1021/acscentsci.9b01006
ACS Cent. Sci. XXXX, XXX, XXX−XXX